Progress In Electromagnetics Research C, Vol. 160, 120–132, 2025 PIER C

(Received 31 July 2025, Accepted 10 September 2025, Scheduled 26 September 2025)

Radar Maneuvering Target Detection and Motion Parameter Estimation Based on KT-SPCFCRD

Aihua Li[1], Wei Liu[1], Yuhang Wang[2], Hao Wang[2, 3, *],
Wenwen Xu[2], and Jianyin Cao[2]

[1]*Beijing Institute of Remote Sensing Equipment, Beijing 100854, China*
[2]*School of Electronic and Optical Engineering*
Nanjing University of Science and Technology, Nanjing 210094, China
[3]*Nanhu Laboratory, Zhejiang 314051, China*

ABSTRACT: Long-time coherent integration (LTCI) is an effective method for maneuvering target detection, as it accumulates signal energy over a long observation period, thereby enhancing the signal-to-noise ratio (SNR). However, as the observation duration increases, range migration (RM) and Doppler frequency migration (DFM) occur, which degrade integration performance. To this end, a scaling factor is first introduced into the parameterized centroid frequency–chirp rate distribution (PCFCRD) algorithm, thereby yielding the scaled PCFCRD (SPCFCRD), which enables flexible adjustment of the chirp rate estimation range and resolution. Furthermore, SPCFCRD is combined with the keystone transform (KT) to form the proposed KT-SPCFCRD algorithm. The RM caused by unambiguous velocity is first corrected by KT, after which the residual RM and DFM are further compensated by SPCFCRD to achieve coherent integration. The effectiveness of the proposed algorithm is validated through simulations and real-data analysis. Compared with several representative algorithms, KT-SPCFCRD achieves superior detection performance while maintaining a balanced computational cost.

1. INTRODUCTION

With the widespread deployment of radar systems in increasingly complex environments, the robust detection of maneuvering targets has become a significant technical challenge. These targets typically exhibit low radar cross-section (RCS) values due to their small size or stealth characteristics, leading to weak backscattered echoes that are easily masked by noise or interference [1–3]. To mitigate this issue, long-time coherent integration (LTCI) techniques have been widely employed. By coherently accumulating the received signal over an extended observation period, LTCI can significantly improve signal-to-noise ratio (SNR), thereby enhancing the detectability of weak target echoes [4–6]. However, the motion of maneuvering targets may lead to range migration (RM) and Doppler frequency migration (DFM), which degrade the integration gain in the moving target detection (MTD) algorithm [7–9]. These issues must be effectively addressed to achieve ideal coherent integration.

Existing research on LTCI algorithms has primarily focused on uniformly moving targets [10–12], uniformly accelerated targets [13–15], and targets with jerk [16–18]. In practical scenarios, it is difficult for the target to maintain an ideal radial motion relative to the radar, and a certain level of radial acceleration is almost inevitable. To mitigate the impact of acceleration on coherent integration performance, the integration time is typically limited to a short period [19]. In contrast, the influence of jerk and higher-order motion components is relatively minor, which allows for more flexibility in integration time [20]. However, incorporating the jerk term into the signal model significantly increases the computational cost of LTCI algorithms. Consequently, most current studies on coherent integration for maneuvering targets focus on uniformly accelerated motion to achieve a balance between detection performance and computational efficiency.

For uniformly accelerated targets, existing detection algorithms can be broadly classified into two types. The first category includes algorithms based on multi-dimensional joint parameter search. For example, generalized Radon Fourier transform (GRFT) performs a three-dimensional search to correct RM and extract the target trajectory. Based on estimated parameters, it constructs a matched Doppler filter to compensate for DFM, thereby enabling coherent integration [21]. In addition to GRFT, algorithms such as Radon-fractional Fourier transform (RFRFT) [22] and Radon-Lv's distribution (RLVD) [23] also perform three-dimensional parameter searches to correct RM and extract motion trajectories. RFRFT and RLVD leverage the fact that, under acceleration-induced modulation, slow-time signal can be modeled as a linear frequency modulated (LFM) waveform. Therefore, these algorithms employ joint time-frequency analysis (JTFA) techniques to achieve coherent integration [24, 25]. Although these algorithms provide excellent detection performance, their high computational cost caused by multi-dimensional parameter search remains a significant drawback.

To reduce computational cost, various stepwise processing algorithms have been proposed. These algorithms

---

* Corresponding author: Hao Wang (haowang@njust.edu.cn).

typically begin by correcting the RM, followed by DFM compensation to achieve coherent integration. Representative algorithms include keystone transform and modified GRFT (KT-MGRFT) [20], KT and matched filtering process (KT-MFP) [26], improved axis rotation and FRFT (IAR-FRFT) [27], and modified axis rotation transform and Lv's transform (MART-LVT) [28]. KT performs a scaling operation on the slow-time axis, which corrects the phase terms associated with RM, thereby achieving RM compensation. However, when the Doppler frequency induced by high-speed target motion exceeds the radar's pulse repetition frequency (PRF), velocity ambiguity arises. Under such circumstances, the RM caused by the target's velocity can be decomposed into two components: one resulting from unambiguous velocity and the other caused by velocity ambiguity factor. Since KT can only correct the RM associated with the unambiguous velocity, both KT-MFP and KT-MGRFT need to search for the ambiguity factor to achieve ambiguity compensation (AC). Specifically, KT-MFP constructs a Doppler filter based on searching ambiguity factor and acceleration to compensate for both RM and DFM, thereby enabling coherent integration. In contrast, KT-MGRFT reduces the velocity search in GRFT to a search over the ambiguity factor, thereby narrowing parameter search space and reducing computational cost. Axis-rotation (AR) operation corrects RM by means of axis rotation and is applicable only to uniformly moving targets. Improvements to AR, such as IAR-FRFT and MART-LVT, have been proposed to extend its applicability to uniformly accelerated targets. After RM correction using AR, coherent integration is achieved through JTFA techniques. Compared with search-based approaches, these algorithms provide reduced computational cost while maintaining satisfactory integration performance.

Another type of stepwise processing algorithm achieves coherent integration through correlation functions, such as three-dimensional scaled transform (TDST) and symmetric correlation function-scaled Fourier transform (SAF-SFT) [29, 30]. TDST operates on echoes in the two-dimensional time domain by introducing a delay variable along the slow-time dimension, thereby constructing a three-dimensional correlation function. Two subsequent SFT operations are then performed to compensate for RM and DFM, respectively, thereby enabling accurate parameter estimation and coherent integration. In contrast, SAF-SFT introduces a delay variable in the fast-time frequency domain and reduces the three-dimensional correlation function to two-dimensional by summation. An SFT is first applied to coherent integration to estimate velocity and range. Subsequently, acceleration estimation and further coherent integration are performed through an additional SAF and SFT operation. Compared with TDST, SAF-SFT offers lower computational cost but exhibits relatively weaker detection performance.

In [31], a novel JTFA algorithm, termed parameterized centroid frequency–chirp rate distribution (PCFCRD), was proposed for parameter estimation of LFM signals. This algorithm exhibits superior noise robustness relative to several conventional algorithms, thereby making it suitable for estimating the motion parameters of maneuvering targets. However, its chirp-rate estimation accuracy is constrained by radar system parameters. To overcome this limitation, a scaled PCFCRD (SPCFCRD) algorithm is introduced by incorporating a scaling factor to flexibly adjust the resolution and range of chirp rate estimation. Building upon this, the present paper proposes a novel algorithm for maneuvering target detection, termed KT-SPCFCRD, which integrates SPCFCRD with KT. RM introduced by unambiguous velocity is first corrected using the KT, after which the residual RM and DFM are compensated via SPCFCRD, thereby enabling coherent integration. The effectiveness of the algorithm is validated through simulations and real-data processing. Compared with several representative algorithms, KT-SPCFCRD achieves superior detection performance with moderate computational cost.

The rest of this paper is organized as follows. Section 2 presents the signal model. Section 3 provides a detailed description of KT-SPCFCRD. Section 4 presents experimental results based on both simulation and real data. Finally, conclusions are drawn in Section 5.

2. BACKGROUND

Suppose that the radar transmits an LFM signal as follows

$$s_t(t) = \text{rect}\left(\frac{t}{T_p}\right) \exp\left(\text{j}\pi\mu t^2\right) \exp\left(\text{j}2\pi f_c t\right), \tag{1}$$

where $\text{rect}(x) = \begin{cases} 1, & |x| \le 1/2 \\ 0, & |x| > 1/2 \end{cases}$ denotes the rectangle window function; t denotes the fast time variable; T_P denotes the pulse duration; μ and f_c denote the frequency modulated rate and carrier frequency of the LFM waveform, respectively. After pulse compression (PC), the received signal of radar can be expressed as

$$s_p\left(t, t_m\right) = A\text{sinc}\left\{B\left[t - \frac{2R\left(t_m\right)}{c}\right]\right\} \exp\left[-\text{j}\frac{4\pi f_c}{c}R(t_m)\right], \tag{2}$$

where $\text{sinc}(x) = \sin(\pi x)/\pi x$; c denotes the speed of light; A and B denote the signal amplitude and bandwidth, respectively; $R(t_m)$ denotes the instantaneous slant range between the radar and target; $t_m = mT_r(m = 0, ..., M-1)$ denotes the slow time variable; T_r denotes the pulse repetition interval; and M denotes the pulse number.

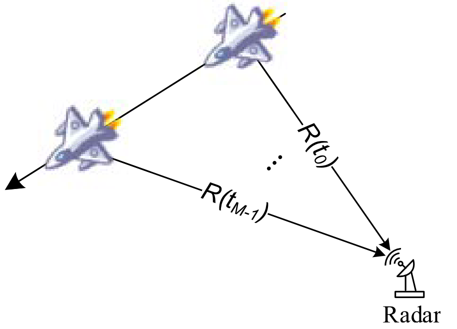

FIGURE 1. Geometry relationship between the radar and the maneuvering target.

Figure 1 illustrates the geometric relationship between the radar and a maneuvering target. This study focuses on the radial component of the target motion, which directly determines the phase of the received signal. Based on the Weierstrass approximation theorem, the phase term is approximated by a polynomial of sufficient order [20]. Usually, the impact of phase terms beyond the second order can be effectively mitigated by restricting the integration time T, as discussed in Section 3.4. Accordingly, $R(t_m)$ can be approximated as

$$R(t_m) = R_0 + vt_m + \frac{1}{2}at_m^2, \tag{3}$$

where R_0, v, and a denote the initial radial range, velocity, and acceleration, respectively.

When velocity ambiguity occurs, $R(t_m)$ can be rewritten as

$$R(t_m) = R_0 + (v_0 + nv_m)\, t_m + \frac{1}{2}at_m^2, \tag{4}$$

where n denotes the ambiguity factor; $v_m = \lambda f_p/2$ denotes the blind velocity; $\lambda = c/f_c$ denotes the signal wavelength; and $v_0 = \mathrm{mod}(v, v_m)$ denotes the unambiguous velocity.

Substituting (4) into (2) yields

$$\begin{aligned} & s_p\left(t, t_m\right) \\ = \; & A_0 \mathrm{sinc}\left\{B\left[t - \frac{2\left(R_0 + v_0 t_m + nv_m t_m + at_m^2/2\right)}{c}\right]\right\} \\ & \times \exp\left[-\mathrm{j}\frac{4\pi}{\lambda}\left(R_0 + v_0 t_m + nv_m t_m + \frac{1}{2}at_m^2\right)\right], \end{aligned} \tag{5}$$

where $\exp(-\mathrm{j}4\pi nv_m t_m/\lambda) = \exp(-\mathrm{j}4\pi nm/2) = 1$. Accordingly, (5) can be simplified as

$$\begin{aligned} & s_p\left(t, t_m\right) \\ = \; & A_0 \mathrm{sinc}\left\{B\left[t - \frac{2\left(R_0 + v_0 t_m + nv_m t_m + at_m^2/2\right)}{c}\right]\right\} \\ & \times \exp\left[-j\frac{4\pi}{\lambda}\left(R_0 + v_0 t_m + \frac{1}{2}at_m^2\right)\right], \end{aligned} \tag{6}$$

As shown in (6), the peak of the echo signal shifts with respect to slow time. When this shift exceeds the range resolution (i.e., $\Delta\mathrm{RM} = vT + aT^2/2 > c/2B$), RM occurs.

The instantaneous Doppler frequency under acceleration is given by

$$f_{\mathrm{d}}\left(t_m\right) = -\frac{2}{\lambda}\frac{\mathrm{d}\left[\left(R_0 + v_0 t_m + at_m^2/2\right)\right]}{\mathrm{d}t_m} = -\frac{2}{\lambda}\left(v_0 + at_m\right). \tag{7}$$

It can be observed from (7) that the target Doppler frequency is no longer constant but varies as a function of acceleration. When this variation exceeds the Doppler resolution (i.e., $\Delta\mathrm{DFM} = 2aT/\lambda > 1/T$), DFM occurs.

3. PRINCIPLE OF KT-SPCFCRD

This section first introduces the principle of SPCFCRD, followed by a description of the KT-SPCFCRD for RM and DFM correction.

3.1. Principle of SPCFCRD

The LFM signal conforms to the model

$$s_L\left(t_L\right) = A_{L0} \exp\left[\mathrm{j}2\pi\left(f_{0L}t_L + \frac{1}{2}\gamma t_L^2\right)\right], \tag{8}$$

where A_L, t_L, f_{0L}, and γ denote the amplitude, time variable, centroid frequency, and chirp rate of the signal, respectively.

Based on CICPF [32], a novel correlation function is introduced and defined as

$$\begin{aligned} & R_L\left(t_L, \tau\right) \\ = \; & s_L\left[t_L + \left(\tau + \frac{h}{2}\right)\right] s_L\left[t_L - \left(\tau + \frac{h}{2}\right)\right] \\ = \; & A_{L0}^2 \exp\left\{\mathrm{j}2\pi\left[2f_{0L}t_L + \gamma t_L^2 + \gamma\left(\tau + \frac{h}{2}\right)^2\right]\right\}, \end{aligned} \tag{9}$$

where τ and h denote the delay variable and constant delay, respectively. The requirements for both the delay variable and constant delay can be satisfied by incorporating historical data.

NUFFT is applied to achieve energy concentration along the delay variable dimension, which can be expressed as

$$\begin{aligned} & R_L\left(t_L, f_\tau\right) \\ = \; & \int R\left(t_L, \tau\right) \exp\left[-\mathrm{j}2\pi\xi f_\tau\left(\tau + \frac{h}{2}\right)^2\right] \mathrm{d}\tau \\ = \; & A_{L1} \exp\left[\mathrm{j}2\pi\left(2f_{0L}t_L + \gamma t_L^2\right)\right] \delta\left(f_\tau - \xi\gamma\right), \end{aligned} \tag{10}$$

where A_{L1} is the amplitude, f_τ the scaled frequency with respect to τ, and ξ the introduced scaling factor. A detailed analysis of the scaling factor will be presented in Section 3.4.

In (10), the energy along the delay variable axis is effectively concentrated. However, due to the presence of t_L^2 in the signal, the energy along the time dimension cannot be properly focused using the fast Fourier transform (FFT). Therefore, the terms related to t_L^2 need to be eliminated first by dechirp processing (DP), followed by coherent integration using FFT, i.e.,

$$\begin{aligned} R_L\left(f_{t_L}, f_\tau\right) & = \mathrm{FFT}_{t_L}\left[R_N\left(t_L, f_\tau\right) \exp\left(-\mathrm{j}2\pi\frac{f_\tau}{\xi}t_L^2\right)\right] \\ & = A_{L2}\delta\left(f_{t_L} - 2f_{0L}\right)\delta\left(f_\tau - \xi\gamma\right), \end{aligned} \tag{11}$$

where A_{L2} denotes the amplitude, $\mathrm{FFT}_{t_L}[\cdot]$ the FFT operation with respect to t_L, and f_{t_L} the frequency with respect to t_L. From (11), it can be observed that the SPCFCRD achieves coherent integration in the $f_{t_L} - f_\tau$ plane.

3.2. RM Correction via KT

Applying the FFT to (5) with respect to t yields

$$s_p\left(f,t_m\right)=A_0\,\mathrm{rect}\left(\frac{f}{B}\right)\exp\left(-\mathrm{j}\frac{4\pi f}{c}nv_mt_m\right)$$
$$\times\exp\left[-\mathrm{j}\frac{4\pi\left(f+f_c\right)}{c}\left(R_0+v_0t_m+\frac{1}{2}at_m^2\right)\right]\quad(12)$$

where A_0 is the amplitude, and f is the range frequency. As shown in (12), RM originates from the coupling between f and t_m.

The KT eliminates the RM caused by unambiguous velocity v_0 through a scaling transformation, expressed as

$$t_m=\frac{f_c}{f+f_c}t'_m,\quad(13)$$

where t'_m is the scaled slow time.

Substituting (13) into (12) yields

$$\begin{aligned}s_{\mathrm{KT}}\left(f,t'_m\right)&=A_0\,\mathrm{rect}\left(\frac{f}{B}\right)\exp\left[-\mathrm{j}\frac{4\pi}{\lambda}\left(\frac{f}{f+f_c}\right)nv_mt'_m\right]\\&\quad\times\exp\left[-\mathrm{j}\frac{4\pi\left(f+f_c\right)}{c}R_0\right]\exp\left(-\mathrm{j}\frac{4\pi}{\lambda}v_0t'_m\right)\\&\quad\times\exp\left[-\mathrm{j}\frac{2\pi}{\lambda}\left(\frac{f_c}{f+f_c}\right)at'^2_m\right].\end{aligned}\quad(14)$$

Under narrowband environment $f \ll f_c$, we have $f_c/(f_c+f)\simeq 1-f/f_c$ [20, 26]. Thus, (14) can be rewritten as

$$\begin{aligned}s_{\mathrm{KT}}\left(f,t'_m\right)&=A_0\,\mathrm{rect}\left(\frac{f}{B}\right)\exp\left[-\mathrm{j}\frac{4\pi}{\lambda}\left(\frac{f}{f+f_c}\right)nv_mt'_m\right]\\&\quad\times\exp\left[-\mathrm{j}\frac{4\pi\left(f+f_c\right)}{c}R_0\right]\exp\left(-\mathrm{j}\frac{4\pi}{\lambda}v_0t'_m\right)\\&\quad\times\exp\left(\mathrm{j}\frac{2\pi f}{c}at'^2_m\right)\exp\left(-\mathrm{j}\frac{2\pi}{\lambda}at'^2_m\right)\end{aligned}\quad(15)$$

In (15), the coupling between f and t_m is removed, which effectively corrects RM. Nevertheless, with respect to long-range surveillance radar, the range resolution is relatively low, and the integration time is limited; therefore, the RM caused by acceleration can be neglected [27, 28]. Therefore, (15) can be simplified as

$$\begin{aligned}&s_{\mathrm{KT}}\left(f,t'_m\right)\\&=A_0\,\mathrm{rect}\left(\frac{f}{B}\right)\exp\left[-\mathrm{j}\frac{4\pi}{\lambda}\left(R_0+v_0t'_m+\frac{1}{2}at'^2_m\right)\right]\\&\quad\times\exp\left(-\mathrm{j}\frac{4\pi f}{c}R_0\right)\exp\left[-\mathrm{j}\frac{4\pi}{\lambda}\left(\frac{f}{f+f_c}\right)nv_mt'_m\right]\end{aligned}\quad(16)$$

3.3. Integration via SPCFCRD

In (16), the RM induced by velocity ambiguity and the DFM resulting from acceleration remain uncorrected and need to be compensated. To enable AC, all possible ambiguity factors n_t are iteratively evaluated to construct the phase compensation function, which is given by

$$H_1\left(n_t;f,t'_m\right)=\exp\left[\mathrm{j}\frac{4\pi}{\lambda}\left(\frac{f}{f+f_c}\right)n_tv_mt'_m\right]\quad(17)$$

When $n_t=n$, multiplying (16) by (17) yields

$$\begin{aligned}s^{n_t}_{\mathrm{KT}}\left(f,t'_m\right)&=A_0\,\mathrm{rect}\left(\frac{f}{B}\right)\exp\left(-\mathrm{j}\frac{4\pi f}{c}R_0\right)\\&\quad\times\exp\left[-\mathrm{j}\frac{4\pi}{\lambda}\left(R_0+v_0t'_m+\frac{1}{2}at'^2_m\right)\right]\end{aligned}\quad(18)$$

Applying the inverse FFT (IFFT) to (18) with respect to f yields

$$\begin{aligned}s^{n_t}_{\mathrm{KT}}\left(t,t_m\right)&=A_0\,\mathrm{sinc}\left[B\left(t-\frac{2R_0}{c}\right)\right]\\&\quad\times\exp\left[-\mathrm{j}\frac{4\pi}{\lambda}\left(R_0+v_0t'_m+\frac{1}{2}at'^2_m\right)\right],\end{aligned}\quad(19)$$

As shown in (19), the RM is fully corrected, leading to the concentration of signal energy within a single range cell. To determine the target's range cell while achieving coherent integration via PCFCRD, a novel correlation function is introduced, i.e.,

$$\begin{aligned}&R^{n_t}_p\left(t,t'_m,\tau\right)\\&=s^{n_t}_{\mathrm{KT}}\left[t,t'_m+\left(\tau+\frac{h}{2}\right)\right]s^{n_t}_{\mathrm{KT}}\left[t,t'_m-\left(\tau+\frac{h}{2}\right)\right]\\&=A_1\left\{\mathrm{sinc}\left[B\left(t-\frac{2R_0}{c}\right)\right]\right\}^2\exp\left(-\mathrm{j}\frac{8\pi}{\lambda}v_0t'_m\right)\\&\quad\times\exp\left(-\mathrm{j}\frac{4\pi}{\lambda}at'^2_m\right)\exp\left[-\mathrm{j}\frac{4\pi}{\lambda}a\left(\tau+\frac{h}{2}\right)^2\right],\end{aligned}\quad(20)$$

where $A_1=A_0^2\exp(-\mathrm{j}8\pi R_0/\lambda)$ is the amplitude. The NUFFT is applied to achieve signal concentration along the delay variable dimension, which can be expressed as

$$\begin{aligned}&R^{n_t}_p\left(t,t'_m,f_\tau\right)\\&=\int R^{n_t}_p\left(t,t'_m,\tau\right)\exp\left[-\mathrm{j}2\pi\xi f_\tau\left(\tau+\frac{h}{2}\right)^2\right]\mathrm{d}\tau\\&=A_2\left\{\mathrm{sinc}\left[B\left(t-\frac{2R_0}{c}\right)\right]\right\}^2\exp\left(-\mathrm{j}\frac{8\pi}{\lambda}v_0t'_m\right)\\&\quad\times\exp\left(-\mathrm{j}\frac{4\pi}{\lambda}at'^2_m\right)\delta\left(f_\tau+\frac{2a\xi}{\lambda}\right)\end{aligned}\quad(21)$$

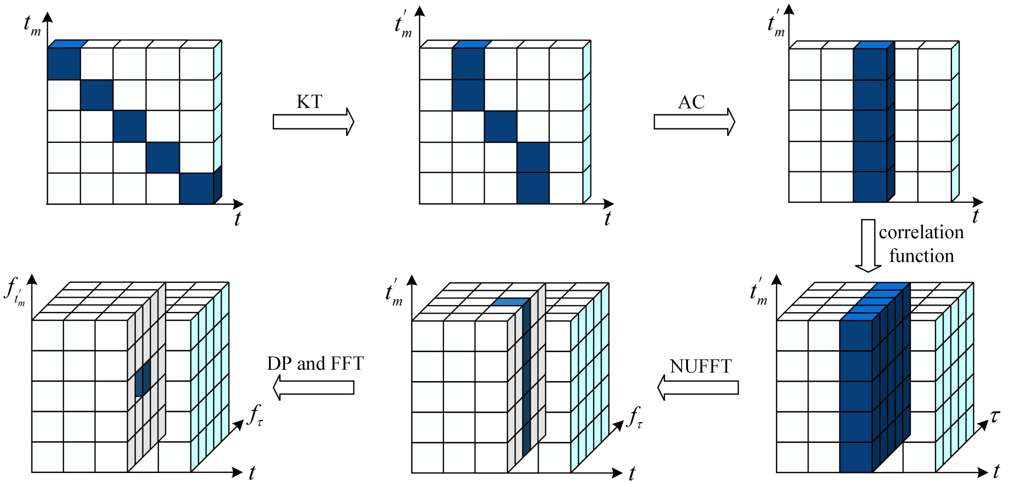

FIGURE 2. Process of signal energy concentration.

where A_2 denotes the amplitude.

Subsequently, coherent integration is achieved via DP and FFT with respect to t'_m, i.e.,

$$\begin{aligned} &R_s^{n_t}\left(t, f_{t'_m}, f_\tau\right) \\ =\ &\text{FFT}_{t'_m}\left[R_p^{n_t}\left(t, t'_m, \tau\right)\exp\left(-\text{j}2\pi\frac{f_\tau}{\xi}t'^2_m\right)\right] \\ =\ &A_3\left\{\text{sinc}\left[B\left(t-\frac{2R_0}{c}\right)\right]\right\}^2\delta\left(f_{t'_m}+\frac{4v_0}{\lambda}\right) \\ &\times\delta\left(f_\tau+\frac{2a\xi}{\lambda}\right) \end{aligned} \tag{22}$$

where A_3 represents the amplitude. From (22), it is observed that the result exhibits a unique peak at $(2R_0/c, -4v_0/\lambda, -2a\xi/\lambda)$. Based on this, the target is detected if the ratio of the peak value to noise exceeds a given threshold. The process of obtaining acceleration and ambiguity factor estimates can be expressed as

$$\left(a_e = -\frac{\lambda f_\tau}{2\xi}, n_e\right) = \underset{n_t, t, f_{t'_m}, f_\tau}{\arg\max}\left|R_s^{n_t}\left(t, f_{t'_m}, f_\tau\right)\right| \tag{23}$$

where a_e and n_e denote the estimated acceleration and ambiguity factor, respectively. The process of signal energy concentration is depicted in Fig. 2, in which the dark shading corresponds to regions of signal peaks.

3.4. Some Remarks

Remark 1: In (11), by introducing the scaling factor ξ, the signal energy becomes concentrated at $f_\tau = \xi\gamma$. Accordingly, the estimation resolution and range of chirp rate are given by $f_{\tau-\max}/L\xi$ and $[-f_{\tau-\max}/2\xi, f_{\tau-\max}/2\xi]$, respectively, where L is the length of t_L, and $f_{\tau-\max}$ is the maximum value of f_τ. *Remark 2*: In the process of constructing the correlation function in (20), the phase term related to velocity is doubled. As a result, the Doppler frequency corresponding to the target's unambiguous velocity is also doubled. Therefore, when $|v_0| > v_m/4$, SPCFCRD fails to accurately estimate the unambiguous velocity. To overcome this limitation, a phase compensation function can be constructed based on the estimated ambiguity factor and acceleration, and applied to (16) to correct the RM and DFM, i.e.,

$$\begin{aligned} H_2\left(n_e, a_e; f, t'_m\right) &= \exp\left[\text{j}\frac{4\pi}{\lambda}\left(\frac{f}{f+f_c}\right)n_e v_m t'_m\right] \\ &\quad\times\exp\left(\text{j}\frac{2\pi}{\lambda}a_e t'^2_m\right) \end{aligned} \tag{24}$$

When $n_e = n$ and $a_e = a$, multiplying (16) and (24) yields

$$\begin{aligned} s_p\left(f, t'_m\right) &= A_0\,\text{rect}\left(\frac{f}{B}\right)\exp\left(-\text{j}\frac{4\pi f}{c}R_0\right) \\ &\quad\times\exp\left[-\text{j}\frac{4\pi}{\lambda}\left(R_0+v_0 t'_m\right)\right] \end{aligned} \tag{25}$$

Subsequently, coherent integration is achieved by applying IFFT with respect to f and FFT with respect to t'_m, yielding

$$s_p\left(t, t_m\right) = A_4\text{sinc}\left[B\left(t-\frac{2R_0}{c}\right)\right]\delta\left(f_{t'_m}+\frac{2v_0}{\lambda}\right) \tag{26}$$

where A_4 denotes the amplitude.

In (26), the unambiguous velocity can be obtained through peak detection.

Remark 3: For targets with jerk, the RM and DFM cannot be effectively corrected using KT-SPCFCRD when the jerk is large. The following section analyzes the applicability conditions of KT-SPCFCRD in the presence of jerk.

Assume that the target has a jerk denoted as j. Accordingly, $R(t_m)$ can be approximated as

$$R(t_m) = R_0 + vt_m + \frac{1}{2}at_m^2 + \frac{1}{6}jt_m^3. \tag{27}$$

The instantaneous Doppler frequency is given by

$$f_{\text{d,jerk}}\left(t_m\right) = \frac{2}{\lambda}\cdot\frac{\text{d}\left(jt_m^3/6\right)}{\text{d}t_m} = \frac{jt_m^2}{\lambda}. \tag{28}$$

To achieve coherent integration, the Nonlinear RM (NRM) and DFM introduced by jerk must remain within a single resolution cell, i.e.,

$$\begin{cases} \Delta \text{NRM}_{\text{jerk}} = \frac{1}{6} j T^3 < \frac{c}{2B} \\ \Delta \text{DFM}_{\text{jerk}} = \frac{j T^2}{\lambda} < \frac{1}{T} \end{cases}. \tag{29}$$

Therefore, the coherent integration time is limited by

$$\begin{cases} T_{\text{NRM}} < \sqrt[3]{\frac{6(c/2B)}{j}} \\ T_{\text{DFM}} < \sqrt[3]{\frac{\lambda}{j}} \end{cases}. \tag{30}$$

Typically, in radar systems, T_{DFM} is more restrictive than T_{NRM}, and it is generally satisfied in practice. *Remark 4*: As a linear transformation, the KT does not introduce cross terms in multi-target scenarios [14]. Meanwhile, PCFCRD has been demonstrated in [31] to exhibit strong suppression of cross terms. Therefore, KT-SPCFCRD inherits these advantages and achieves excellent multi-target resolution performance, as will be further illustrated in Section 4.2.

3.5. Detailed Procedure of KT-SPCFCRD

The overall flowchart of KT-SPCFCRD is illustrated in Fig. 3, and the procedure is summarized as follows:

Step 1: Perform pulse compression on the received signal $s_r(t, t_m)$, yielding $s_p(t, t_m)$;

Step 2: Perform the FFT on $s_p(t, t_m)$ with respect to t, yielding $s_p(f, t_m)$;

Step 3: Apply the KT to $s_p(f, t_m)$ to correct RM, yielding $s_{\text{KT}}(f, t'_m)$;

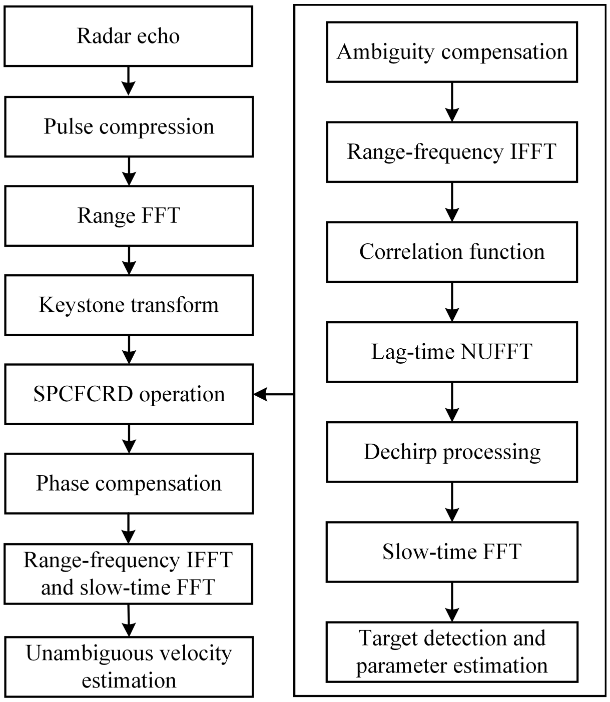

FIGURE 3. Flowchart of KT-SPCFCRD.

Step 4: Construct a phase compensation function based on the ambiguity factor n_e to mitigate velocity ambiguity in $s_{\text{KT}}(f, t'_m)$, yielding $s_{\text{KT}}^{n_t}(f, t'_m)$. Subsequently, apply the IFFT with respect to f to obtain $s_{\text{KT}}^{n_t}(t, t'_m)$.

Step 5: Construct the correlation function $R_p^{n_t}(t, t'_m, \tau)$ using $s_{\text{KT}}^{n_t}(t, t'_m)$.

Step 6: Apply the NUFFT along the delay variable dimension of $R_p^{n_t}(t, t'_m, \tau)$ to achieve energy focusing in the delay-frequency domain, resulting in $R_p^{n_t}(t, t'_m, f_\tau)$.

Step 7: Perform the DP on $R_p^{n_t}(t, t'_m, f_\tau)$, followed by an FFT with respect to t'_m to obtain $R_p^{n_t}(t, f_{t'_m}, f_\tau)$.

Step 8: Peak detection is then performed on $R_p^{n_t}(t, f_{t'_m}, f_\tau)$ to detect the target and estimate its range r_e, ambiguity factor n_e, and acceleration a_e.

Step 9: Use the estimated ambiguity factor and acceleration to construct a phase compensation function that corrects the RM and DFM in $s_{\text{KT}}(f, t'_m)$. Finally, apply IFFT with respect to f and FFT with respect to t'_m to achieve coherent integration, and further detect the target within range r_e.

3.6. Computational Cost

This section compares RFRFT [22], GRFT [21], KT-MGRFT [20], MART-LVT [28], and SAF-SFT [30], with computational cost evaluated by counting complex multiplications. The number of the pulses, range cells, searching fractional orders, searching rotation angles, searching velocities, searching ambiguity factors, and accelerations are denoted by M, N, N_β, N_θ, N_v, N_n, and N_a, respectively. The RFRFT determines target trajectories by conducting a search over the range, velocity, and acceleration dimensions, where the FRFT is employed along each candidate trajectory to accumulate signal energy. This process results in a computational cost of $\text{O}[N_r N_n N_v N_a (N_\beta M \log_2 M)]$. Similar to RFRFT, GRFT determines target trajectories by performing a search over range, velocity, and acceleration, followed by phase compensation and summation for coherent integration. This procedure leads to a computational cost of $\text{O}(N_r N_v N_n N_a M)$. For KT-MGRFT, the KT can be efficiently implemented using the chirp-Z transform (CZT)-based SFT and IFFT, resulting in a computational cost of $\text{O}(4MN \log_2 N)$. The MGRFT performs trajectory searching over the range, ambiguity factor, and acceleration dimensions, and integrates signal energy using the FFT, leading to a computational cost of $\text{O}(N_r N_n N_a M \log_2 M)$. Therefore, the computational cost of KT-MGRFT is about $\text{O}(N_r N_n N_a M \log_2 M)$. MART-LVT mainly consists of two stages: MART operation, which has a computational cost of $\text{O}(N_\theta N)$, and LVT operation, with a computational cost of $\text{O}(4M^2 \log_2 M)$. Therefore, the total computational cost of MART-LVT is about $\text{O}[N_\theta N (4M^2 \log_2 M)]$. The SAF-SFT involves two SAF-SFT operations, with computational costs of $\text{O}[M^3 + MN(3 \log_2 M + \log_2 N)]$ and $\text{O}(M^2 + 4M^2 \log_2 M)$, respectively. The main steps and their corresponding computational costs of KT-SPCFCRD are as follows: AC with $\text{O}(N_n MN)$, correlation function with $\text{O}(N_n M^2 N)$, NUFFT with $\text{O}(2N_n M^2 N \log_2 M)$, DP with $\text{O}(N_n M^2 N)$, and FFT

TABLE 1. Computational cost of each algorithm.

Algorithm	Computation cost
RFRFT	$\mathrm{O}(N_n M^5 \log_2 M)$
GRFT	$\mathrm{O}(N_n M^4)$
KT-MGRFT	$\mathrm{O}(N_n M^3 \log_2 M)$
MART-LVT	$\mathrm{O}(4M^4 \log_2 M)$
SAF-SFT	$\mathrm{O}(M^3)$
Proposed KT-SPCFCRD	$\mathrm{O}(3N_n M^3 \log_2 M)$

with $\mathrm{O}(N_n M^2 N \log_2 M)$. Therefore, the total computational cost of KT-SPCFCRD is about $\mathrm{O}(3N_n M^2 N \log_2 M)$.

Assuming that $N_p = N_\theta = N_v = N_a = N = M$, the computational costs of the compared algorithms are summarized in Table 1. Taking $N_n = 10$ as an illustrative case, Fig. 4 presents how the computational cost evolves as the number of pulses increases from 32 to 1024. According to Table 1 and Fig. 4, KT-SPCFCRD achieves a significant reduction in computational burden compared with RFRFT, GRFT, and MART-LVT. Its computational cost is comparable to that of KT-MGRFT, though higher than SAF-SFT.

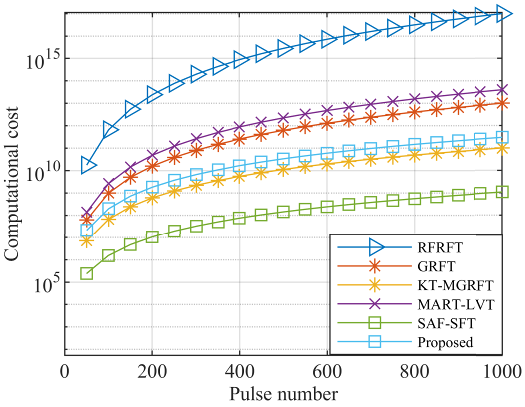

FIGURE 4. Computational cost of each algorithm.

4. EXPERIMENTAL RESULTS

This section validates the effectiveness of the proposed algorithm through both simulations and real radar data. The radar system and target parameters employed in the simulations are listed in Tables 2 and 3, respectively.

TABLE 2. Simulation parameters of radar.

Parameters	Value	Parameters	Value
Carrier frequency	3 GHz	Bandwidth	3 MHz
PRF	2 kHz	Sampling frequency	5 MHz
Pulse duration	25 µs	Pulse number	512

TABLE 3. Simulation parameters of targets.

Parameters	Target A	Target B	Target C
SNR after PC	7 dB	7 dB	7 dB
Range	6 km	6 km	6 km
Velocity	710 m/s	720 m/s	710 m/s
Acceleration	30 m/s^2	30 m/s^2	40 m/s^2

4.1. Coherent Integration for a Single Target

In this section, Target A is considered as a single target. In this scenario, the blind velocity is set to 100 m/s, and the target has an ambiguity factor of 3, corresponding to an unambiguous velocity of 10 m/s. The range resolution is 15 m, while the RM induced by acceleration is only 0.98 m, which is smaller than the range resolution and can thus be neglected. This result is consistent with the analysis presented in Section 3.2. As shown in Fig. 5(a), after PC, the signal peak appears as a slanted line in the fast-time versus slow-time plane, indicating significant RM due to target maneuvering. If the echo signal is directly processed using MTD, as illustrated in Fig. 5(b), the signal energy spreads across both the range and Doppler dimensions, thereby preventing effective energy focusing. The parameter estimation results after applying the proposed KT-SPCFCRD algorithm are shown in Figs. 5(c)–(e), where a notable energy concentration is observed. Furthermore, after phase compensation, the MTD result in Fig. 5(f) demonstrates that the target energy is well focused, thereby achieving effective coherent integration.

4.2. Coherent Integration for Multiple Targets

The following simulation aims to verify the multi-target processing capability of the algorithm. The motion parameters of multiple targets are summarized in Table 3. Fig. 6(a) shows the result after PC. Due to the similarity of the motion parameters of the three targets, their motion trajectories are closely intertwined. The simulation results of the proposed algorithm are presented in Figs. 6(b)–(h). In Fig. 6(b), three distinct peaks appear on the acceleration-velocity plane, which verifies the strong cross-term suppression capability of the PCFCRD algorithm. Similarly, the presence of multiple distinct energy peaks in Figs. 6(c)–(f) clearly demonstrates the successful separation of multiple targets. Since Targets A and B share the same ambiguity factor and acceleration, the compensation function constructed based on the estimated parameters aligns both targets in the MTD results, as shown in Fig. 6(g). Overall, the KT-SPCFCRD algorithm demonstrates strong capability in handling multiple targets effectively.

The above simulation scenario mainly considered multiple targets with comparable SNRs. However, when strong and weak targets coexist within the same range cell, separating the aliased multi-target signals becomes more challenging. Moreover, the main-lobe and sidelobes of the strong target's SPCFCRD response may mask weak targets with similar motion parameters. To address this issue, methods such as CLEAN algorithm [33, 34], blind source separation (BSS) algorithm [35], and analytic signal construction-BSS (ASC-BSS) algorithm [36] can be considered to achieve more reliable separation and detection of strong and weak targets.

4.3. Coherent Integration for Real Data

The proposed KT-SPCFCRD algorithm is further validated using real radar data for unmanned aerial vehicle (UAV) target detection, as described in [37]. The radar system parameters and target parameters are listed in Tables 4 and 5. The blind

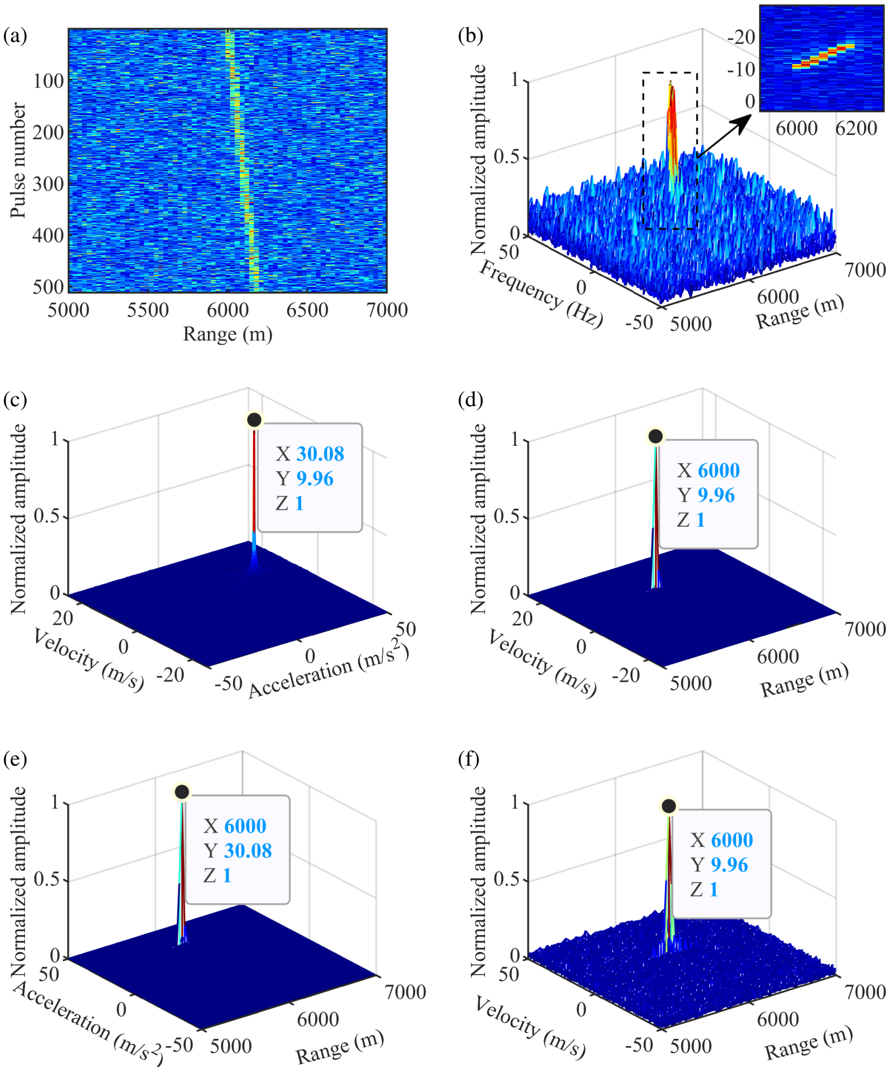

FIGURE 5. Simulation results for a single target. (a) Result after PC. (b) Result after MTD. (c) Velocity-acceleration estimation result. (d) Range-velocity estimation result. (e) Range-acceleration estimation result. (f) MTD result after RM and DFM correction.

TABLE 4. Parameters of radar.

Parameters	Value	Parameters	Value
Carrier frequency	35 GHz	Sampling frequency	80 MHz
PRF	32 kHz	Pulse number	1600

TABLE 5. Parameters of a single target.

Parameters	Value
Range	285 m
Velocity	-40.31 m/s
Acceleration	0.34 m/s^2

speed is 137.14 m/s, and thus the ambiguity factor of the target is 0.

The radar echo after PC is shown in Fig. 7(a), where the target trajectory is submerged in strong ground clutter. The result after moving target indication (MTI) processing is shown in Fig. 7(b), which demonstrates that MTI effectively suppresses ground clutter. Furthermore, as shown in Fig. 7(b), unlike the simulated signal, the real radar data are non-ideally continuous, exhibiting missing pulses and fluctuations in signal amplitude. The simulation results of the proposed algorithm are presented in Figs. 7(c)–(f). It can be observed that, due to the velocity-related phase term being doubled in the AF, the unambiguous velocity estimation result is inaccurate. However, after compensation, the result obtained using the matched filter-based MTD in Fig. 7(f) is close to the actual target parameters. The simulation results validate the effectiveness of the KT-SPCFCRD algorithm for handling real radar data.

4.4. Detection Performance

To evaluate the detection performance under noisy conditions, a constant false alarm rate (CFAR) detector is applied to each algorithm. The simulation parameters are consistent with those listed in Tables 2 and 3. To further demonstrate the effectiveness of the proposed algorithm, it is also compared with the moving target detection (MTD) algorithm. The SNR be-

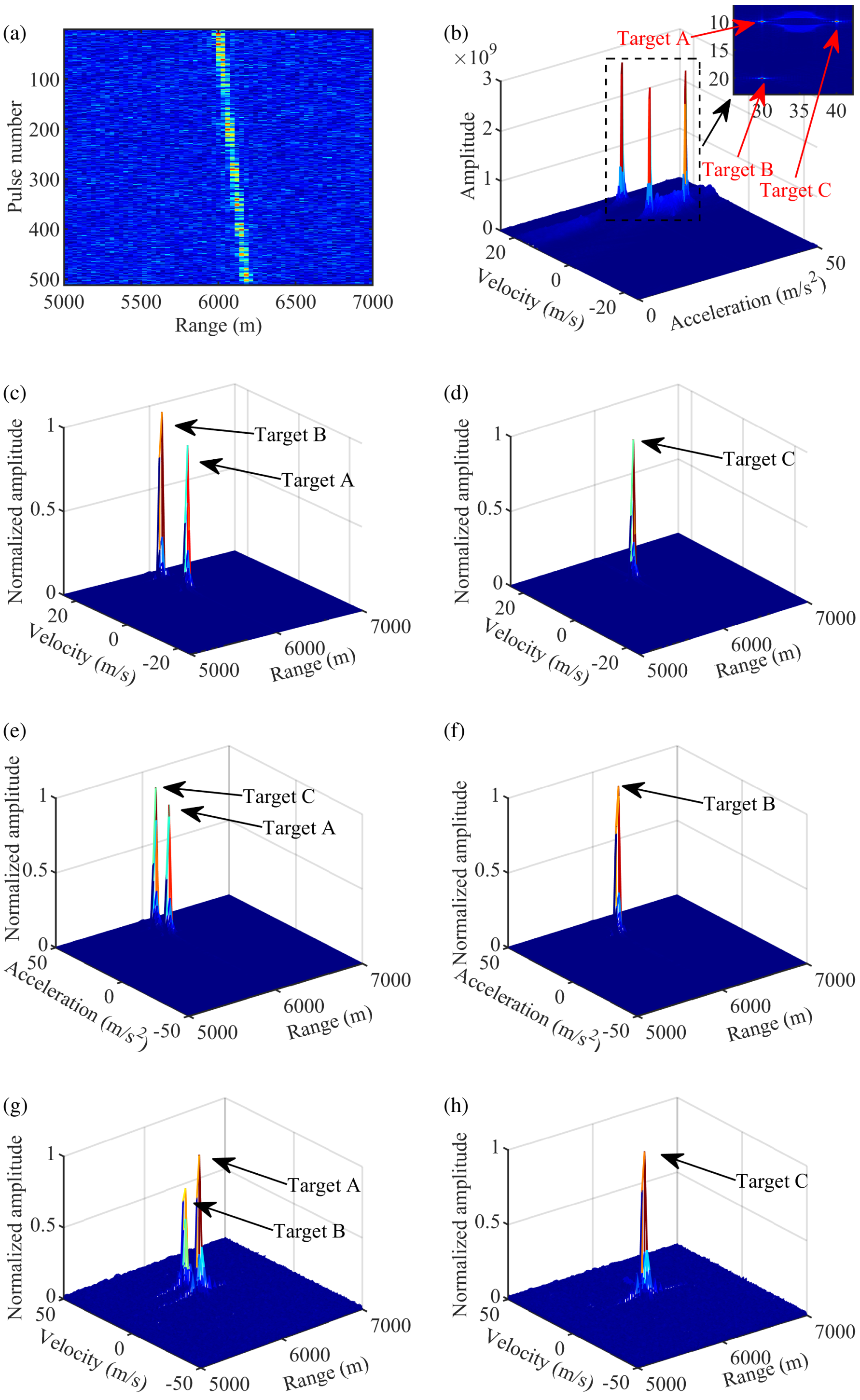

FIGURE 6. Simulation results for multiple targets. (a) Result after PC. (b) Velocity-acceleration estimation result. (c) Range-velocity estimation result of Targets A and B. (d) Range-velocity estimation result of Target A. (e) Range-acceleration estimation result of Targets A and C. (f) Range-acceleration estimation result of Target B. (g) MTD result after RM and DFM correction of Targets A and B. (h) MTD result after RM and DFM correction of Target C.

fore PC ranges from -20 dB to 0 dB, with 500 Monte Carlo trials conducted for each SNR level. Fig. 8 shows the detection probability and root mean square error (RMSE) of motion parameter estimation as functions of SNR for each algorithm, with a false alarm probability of 10^{-6}. As shown in Fig. 8(a), when the detection probability reaches 1, the proposed KT-SPCFCRD achieves approximately 4 dB, 4 dB, 2 dB, 3 dB, 10 dB, and 16 dB lower minimum detectable SNR than RFRFT, MART-LVT, GRFT, KT-MGRFT, SAF-SFT, and MTD algorithms, respectively. A joint analysis of Fig. 4 and Fig. 8(a) indicates that KT-SPCFCRD delivers superior detection performance while maintaining computational cost compa-

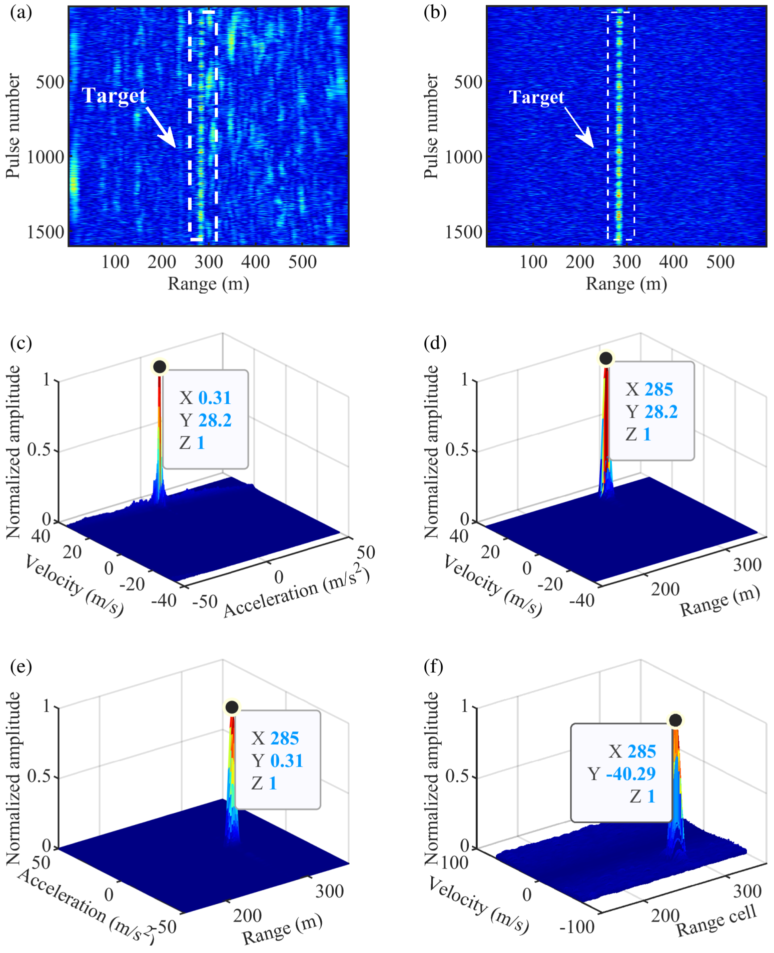

FIGURE 7. Processing results of the real data. (a) Result after PC. (b) Result after MTI. (c) Velocity-acceleration estimation result. (d) Range-velocity estimation result. (e) Range-acceleration estimation result. (f) MTD result after RM and DFM correction.

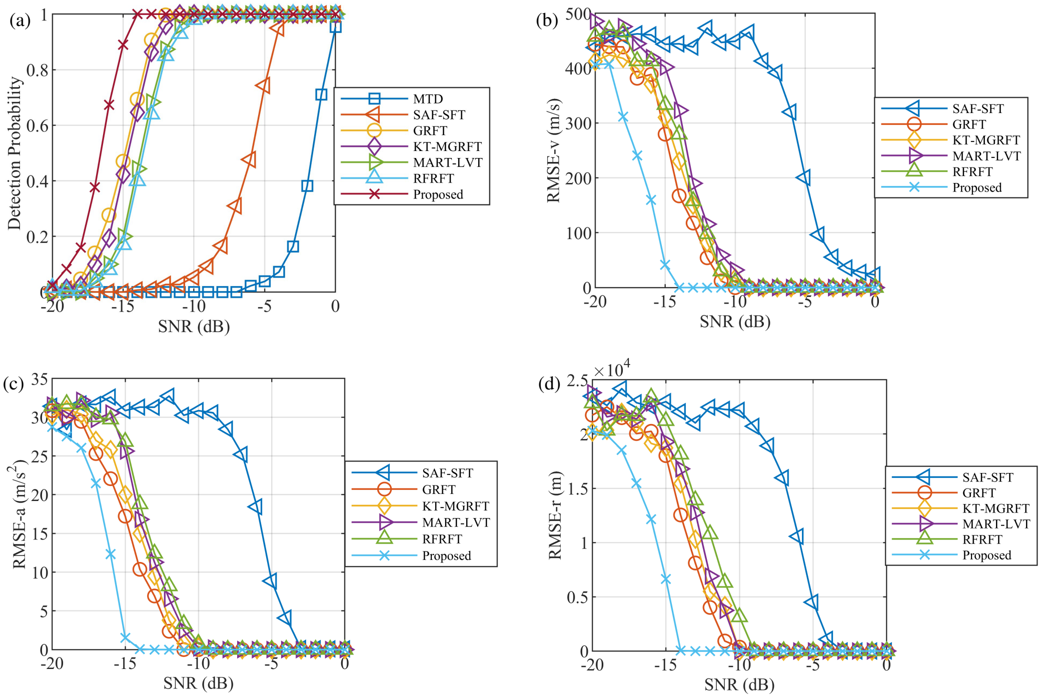

FIGURE 8. Performance evaluation of different algorithms (a) Detection probability. (b) RMSE of velocity estimation. (c) RMSE of acceleration estimation. (d) RMSE of range estimation.

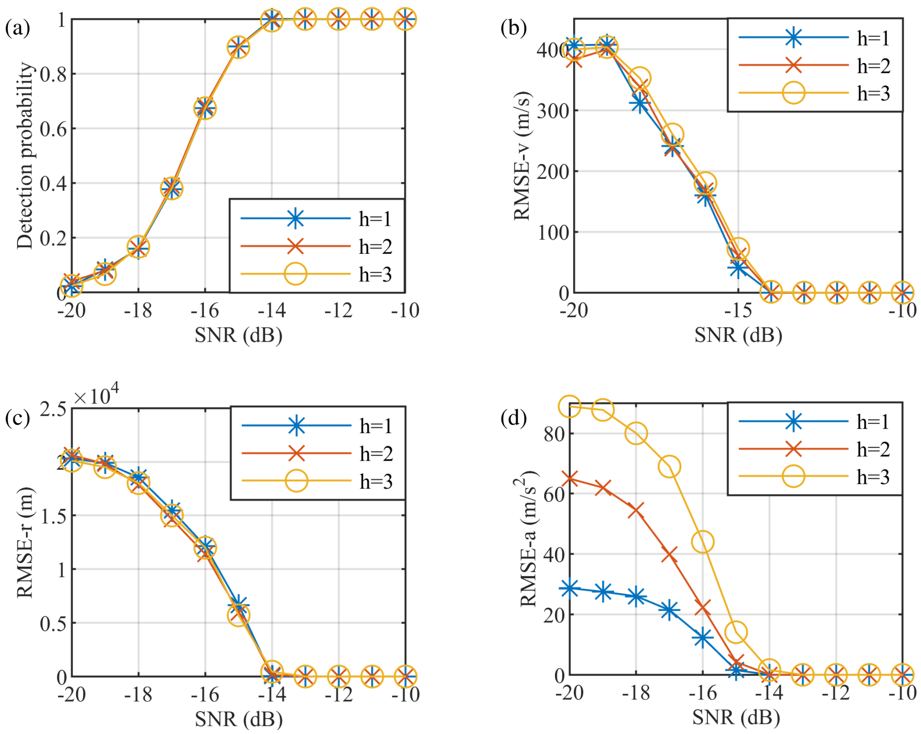

FIGURE 9. Experimental results for targets with different scaling factors. (a) Detection probability. (b) RMSE of velocity estimation. (c) RMSE of range estimation. (d) RMSE of acceleration estimation.

rable to KT-MGRFT. This improvement is primarily attributed to the strong noise robustness of SPCFCRD. Compared with RFRFT, MART-LVT, and GRFT, KT-SPCFCRD provides enhanced detection capability with substantially reduced computational cost. Although SAF-SFT exhibits the lowest computational cost among all algorithms, it also suffers from the poorest detection performance. Moreover, as shown in Figs. 8(b)–(d), KT-SPCFCRD also demonstrates significant improvements in motion parameter estimation accuracy compared with other algorithms, consistent with its superior detection performance.

4.5. Analysis of the Introduced Scaling Factor

In previous simulations, a scaling factor of $\xi = 1$ was used, corresponding to a maximum detectable acceleration of $50\,\mathrm{m/s^2}$ and a resolution of $0.20\,\mathrm{m/s^2}$. To evaluate the impact of the scaling factor on the performance of the proposed algorithm, scaling factors of 2 and 3 are also considered. Under these conditions, the detection performance and the RMSE of motion parameter estimation are analyzed. As shown in Fig. 9, the primary impact of the scaling factor is observed in the RMSE of acceleration estimation, as it directly alters the acceleration estimation range. In contrast, its influence on detection performance, velocity estimation RMSE, and range estimation RMSE is relatively minor. Overall, the scaling factor has minimal impact on the overall performance of the algorithm, while improving its adaptability to different radar system configurations.

5. CONCLUSION

Based on the PCFCRD algorithm, this paper introduces a scaling factor and develops SPCFCRD algorithm, which enables flexible adjustment of the estimation range and resolution of the chirp rate. Subsequently, by combining KT with SPCFCRD, a KT-SPCFCRD-based algorithm for maneuvering target detection and parameter estimation is proposed. This algorithm effectively mitigates the effects of RM and DFM in the echo signal. The effectiveness of the proposed algorithm is demonstrated through theoretical analysis, simulation experiments, and real radar data evaluations. Compared with several representative algorithms, KT-SPCFCRD achieves enhanced detection performance while maintaining moderate computational cost. Future research may focus on extending the algorithm to scenarios where jerk cannot be neglected and on addressing the scale effect (SE) in large time-bandwidth product (LTBP) radars [38, 39]. In addition, effective detection strategies under the coexistence of strong and weak targets, as well as integration with interference and clutter suppression techniques [40–42], will be explored to further enhance radar detection robustness in complex environments.

REFERENCES

[1] Jin, K., G. Li, T. Lai, T. Jin, and Y. Zhao, "A novel long-time coherent integration algorithm for Doppler-ambiguous radar maneuvering target detection," *IEEE Sensors Journal*, Vol. 20, No. 16, 9394–9407, Aug. 2020.

[2] Zhan, M., P. Huang, S. Zhu, X. Liu, G. Liao, J. Sheng, and S. Li, "A modified Keystone transform matched filtering method for space-moving target detection," *IEEE Transactions on Geoscience and Remote Sensing*, Vol. 60, 1–16, 2022.

[3] Xu, Z., G. Wu, G. Li, and G. Zhou, "Fast coherent integration based on time-frequency reversal decoupling transform for maneuvering target detection," *IEEE Transactions on Aerospace and Electronic Systems*, Vol. 60, No. 6, 8805–8822, Dec. 2024.

[4] Sun, Z., X. Li, W. Yi, G. Cui, and L. Kong, "Detection of weak maneuvering target based on Keystone transform and matched filtering process," *Signal Processing*, Vol. 140, 127–138, 2017.

[5] Sun, Z., X. Li, W. Yi, G. Cui, and L. Kong, "A coherent detection and velocity estimation algorithm for the high-speed target based on the modified location rotation transform," *IEEE Journal of Selected Topics in Applied Earth Observations and Remote Sensing*, Vol. 11, No. 7, 2346–2361, Jul. 2018.

[6] Li, X., G. Cui, W. Yi, and L. Kong, "Sequence-reversing transform-based coherent integration for high-speed target detection," *IEEE Transactions on Aerospace and Electronic Systems*, Vol. 53, No. 3, 1573–1580, Jun. 2017.

[7] Zhang, J., T. Su, J. Zheng, and X. He, "Novel fast coherent detection algorithm for radar maneuvering target with jerk motion," *IEEE Journal of Selected Topics in Applied Earth Observations and Remote Sensing*, Vol. 10, No. 5, 1792–1803, May 2017.

[8] Xu, W., Y. Wang, J. Huang, H. Wang, and J. Cao, "SAF-SFT-SRAF-based signal coherent integration method for high-speed target detecting in airborne radar," *Progress In Electromagnetics Research C*, Vol. 154, 183–190, 2025.

[9] Li, S., Y. Wang, B. Wang, G. Battistelli, L. Chisci, and G. Cui, "Efficient dual-scale generalized Radon-Fourier transform detector family for long time coherent integration," *IEEE Transactions on Signal Processing*, Vol. 72, 4237–4252, 2024.

[10] Perry, R. P., R. C. DiPietro, and R. L. Fante, "SAR imaging of moving targets," *IEEE Transactions on Aerospace and Electronic Systems*, Vol. 35, No. 1, 188–200, Jan. 1999.

[11] Zheng, J., T. Su, W. Zhu, X. He, and Q. H. Liu, "Radar high-speed target detection based on the scaled inverse Fourier transform," *IEEE Journal of Selected Topics in Applied Earth Observations and Remote Sensing*, Vol. 8, No. 3, 1108–1119, Mar. 2015.

[12] Huang, P., G. Liao, Z. Yang, X.-G. Xia, J. Ma, and X. Zhang, "An approach for refocusing of ground moving target without target motion parameter estimation," *IEEE Transactions on Geoscience and Remote Sensing*, Vol. 55, No. 1, 336–350, Jan. 2017.

[13] Chen, X., J. Guan, Y. Huang, N. Liu, and Y. He, "Radon-linear canonical ambiguity function-based detection and estimation method for marine target with micromotion," *IEEE Transactions on Geoscience and Remote Sensing*, Vol. 53, No. 4, 2225–2240, Apr. 2015.

[14] Huang, X., L. Zhang, S. Li, and Y. Zhao, "Radar high speed small target detection based on Keystone transform and linear canonical transform," *Digital Signal Processing*, Vol. 82, 203–215, 2018.

[15] Zhang, H. and X. Gao, "Radar detection and parameter estimation of high-speed targets based on RFRT-SoWVD," *Journal of Applied Remote Sensing*, Vol. 16, No. 2, 026515, Jun. 2022.

[16] Li, X., G. Cui, L. Kong, and W. Yi, "Fast non-searching method for maneuvering target detection and motion parameters estimation," *IEEE Transactions on Signal Processing*, Vol. 64, No. 9, 2232–2244, May 2016.

[17] Yu, W., W. Su, and H. Gu, "Ground moving target motion parameter estimation using Radon modified Lv's distribution," *Digital Signal Processing*, Vol. 69, 212–223, Oct. 2017.

[18] Cao, Y.-F., W.-Q. Wang, and S. Zhang, "Long-time coherent integration for high-order maneuvering target detection via zero-trap line extraction," *IEEE Transactions on Aerospace and Electronic Systems*, Vol. 57, No. 6, 4017–4027, Dec. 2021.

[19] Xu, J., J. Yu, Y.-N. Peng, and X.-G. Xia, "Radon-Fourier transform for radar target detection, I: Generalized Doppler filter bank," *IEEE Transactions on Aerospace and Electronic Systems*, Vol. 47, No. 2, 1186–1202, Apr. 2011.

[20] Fang, X., G. Xiao, Z. Cao, R. Min, and Y. Pi, "Migration correction algorithm for coherent integration of low-observable target with uniform radial acceleration," *IEEE Transactions on Instrumentation and Measurement*, Vol. 70, 1–13, 2021.

[21] Xu, J., X.-G. Xia, S.-B. Peng, J. Yu, Y.-N. Peng, and L.-C. Qian, "Radar maneuvering target motion estimation based on generalized Radon-Fourier transform," *IEEE Transactions on Signal Processing*, Vol. 60, No. 12, 6190–6201, Dec. 2012.

[22] Chen, X., J. Guan, N. Liu, and Y. He, "Maneuvering target detection via Radon-fractional Fourier transform-based long-time coherent integration," *IEEE Transactions on Signal Processing*, Vol. 62, No. 4, 939–953, 2014.

[23] Li, X., G. Cui, W. Yi, and L. Kong, "Coherent integration for maneuvering target detection based on Radon-Lv's distribution," *IEEE Signal Processing Letters*, Vol. 22, No. 9, 1467–1471, 2015.

[24] Namias, V., "The fractional order Fourier transform and its application to quantum mechanics," *IMA Journal of Applied Mathematics*, Vol. 25, No. 3, 241–265, Mar. 1980.

[25] Lv, X., G. Bi, C. Wan, and M. Xing, "Lv's distribution: Principle, implementation, properties, and performance," *IEEE Transactions on Signal Processing*, Vol. 59, No. 8, 3576–3591, Aug. 2011.

[26] Huang, P., G. Liao, Z. Yang, X.-G. Xia, J.-T. Ma, and J. Ma, "Long-time coherent integration for weak maneuvering target detection and high-order motion parameter estimation based on Keystone transform," *IEEE Transactions on Signal Processing*, Vol. 64, No. 15, 4013–4026, Aug. 2016.

[27] Rao, X., H. Tao, J. Su, J. Xie, and X. Zhang, "Detection of constant radial acceleration weak target via IAR-FRFT," *IEEE Transactions on Aerospace and Electronic Systems*, Vol. 51, No. 4, 3242–3253, 2015.

[28] Li, X., Z. Sun, W. Yi, G. Cui, and L. Kong, "Radar detection and parameter estimation of high-speed target based on MART-LVT," *IEEE Sensors Journal*, Vol. 19, No. 4, 1478–1486, Feb. 2019.

[29] Zheng, J., H. Liu, J. Liu, X. Du, and Q. H. Liu, "Radar high-speed maneuvering target detection based on three-dimensional scaled transform," *IEEE Journal of Selected Topics in Applied Earth Observations and Remote Sensing*, Vol. 11, No. 8, 2821–2833, Aug. 2018.

[30] Li, X., Z. Sun, W. Yi, G. Cui, L. Kong, and X. Yang, "Computationally efficient coherent detection and parameter estimation algorithm for maneuvering target," *Signal Processing*, Vol. 155, 130–142, 2019.

[31] Zheng, J., H. Liu, and Q. H. Liu, "Parameterized centroid frequency-chirp rate distribution for LFM signal analysis and mechanisms of constant delay introduction," *IEEE Transactions on Signal Processing*, Vol. 65, No. 24, 6435–6447, Dec. 2017.

[32] Su, J., H.-H. Tao, X. Rao, J. Xie, and X.-L. Guo, "Coherently integrated cubic phase function for multiple LFM signals analysis," *Electronics Letters*, Vol. 51, No. 5, 411–413, 2015.

[33] Qian, L., J. Xu, W. Sun, and Y. Peng, "CLEAN based blind speed side lobe (BSSL) suppression in the Radon Fourier Transform (RFT) for multi-target detection," in *2012 IEEE 12th Inter-*

national Conference on Computer and Information Technology, 490–495, Chengdu, China, 2012.

[34] Zhao, Z. and X. Li, "High-speed UAV swarms detection via coherent integration and GTE-based super-resolution method," *IEEE Transactions on Aerospace and Electronic Systems*, Vol. 60, No. 2, 1583–1596, Apr. 2024.

[35] Deng, J., Z. Sun, W. Liu, X. Li, and G. Cui, "Blind source separation-based high-speed weak target coherent detection method under strong target BSSL covering situation," *IEEE Transactions on Aerospace and Electronic Systems*, Vol. 61, No. 3, 7987–7994, Jun. 2025.

[36] Deng, J., Z. Sun, X. Li, and G. Cui, "ASC-BSS-based parameter estimation method for multiple LFM pulses with aliasing effect from passive radar," *IEEE Transactions on Aerospace and Electronic Systems*, Vol. 61, No. 2, 5132–5144, Apr. 2025.

[37] Song, Z., B. Hui, H. Fan, J. Zhou, Y. Zhu, K. Da, X. Zhang, H. Su, W. Jin, Y. Zhang, *et al.*, "A dataset for dim target detection and tracking of aircraft in radar echo sequences," *Sci. Data Bank*, Vol. 1, 2019.

[38] Sun, Z., X. Jiang, H. Zhang, J. Deng, S. Wu, X. Li, and G. Cui, "Joint elimination method of scale effect and range migration/Doppler migration for hypersonic maneuvering target under large time-bandwidth product condition," *Signal Processing*, Vol. 210, 109074, 2023.

[39] Sun, Z., X. Li, G. Cui, W. Yi, and L. Kong, "Hypersonic target detection and velocity estimation in coherent radar system based on scaled radon Fourier transform," *IEEE Transactions on Vehicular Technology*, Vol. 69, No. 6, 6525–6540, Jun. 2020.

[40] Li, J., Z. Sun, X. Yu, Y. Kong, G. Cui, and Z. Xiang, "Intra-pulse forwarding jamming detection and identification framework for airborne radar system under clutter environment," *IEEE Transactions on Aerospace and Electronic Systems*, 2025.

[41] Gao, Y., H. Fan, L. Ren, Z. Liu, Q. Liu, and E. Mao, "Joint design of waveform and mismatched filter for interrupted sampling repeater jamming suppression," *IEEE Transactions on Aerospace and Electronic Systems*, Vol. 59, No. 6, 8037–8050, Dec. 2023.

[42] Liu, Z., H. Ye, Z. Li, Q. Yang, Z. Sun, J. Wu, and J. Yang, "Optimally matched space-time filtering technique for BFSAR nonstationary clutter suppression," *IEEE Transactions on Geoscience and Remote Sensing*, Vol. 60, 1–17, 2022.